LETTERS

Extent, duration and speed of the 2004 Sumatra–Andaman earthquake imaged by the Hi-Net array

Miaki Ishii[1]*, Peter M. Shearer[1]*, Heidi Houston[2] & John E. Vidale[2]

The disastrous Sumatra–Andaman earthquake of 26 December 2004 was one of the largest ever recorded. The damage potential of such earthquakes depends on the extent and magnitude of fault slip. The first reliable moment magnitude estimate[1] of 9.0 was obtained several hours after the Sumatra–Andaman earthquake, but more recent, longer-period, normal-mode analyses have indicated that it had a moment magnitude of 9.3, about 2.5 times larger[2]. Here we introduce a method for directly imaging earthquake rupture that uses the first-arriving compressional wave and is potentially able to produce detailed images within 30 min of rupture initiation. We used the Hi-Net seismic array in Japan as an antenna to map the progression of slip by monitoring the direction of high-frequency radiation. We find that the rupture spread over the entire 1,300-km-long aftershock zone by propagating northward at roughly 2.8 km s^{-1} for approximately 8 minutes. Comparisons with the aftershock areas of other great earthquakes indicate that the Sumatra–Andaman earthquake did indeed have a moment magnitude of ~9.3. Its rupture, in both duration and extent, is the longest ever recorded.

Although aftershocks and an extended P-wave train suggested a 1,200-km-long rupture[3], conventional source modelling using long-period body-wave and surface-wave seismograms constrained the bulk of the slip to the southern portion of the aftershock zone (Fig. 1a). A different approach to mapping the slip exploits the high-frequency energy generated during rupture propagation. Hi-Net, a dense seismic array in Japan[4], consists of about 700 short-period borehole instruments located throughout Japan at ~20 km spacing (Fig. 1b). The array spans distances from 43° to 60° and azimuths from 36° to 47° with respect to the Sumatra–Andaman mainshock epicentre. The P-wave onset of the event is remarkably coherent among different stations in the array (Fig. 1c), but later parts of the P wavetrain are complicated by multiple, overlapping arrivals of seismic energy from different portions of the rupture. Because changes in the source location cause changes in the relative arrival

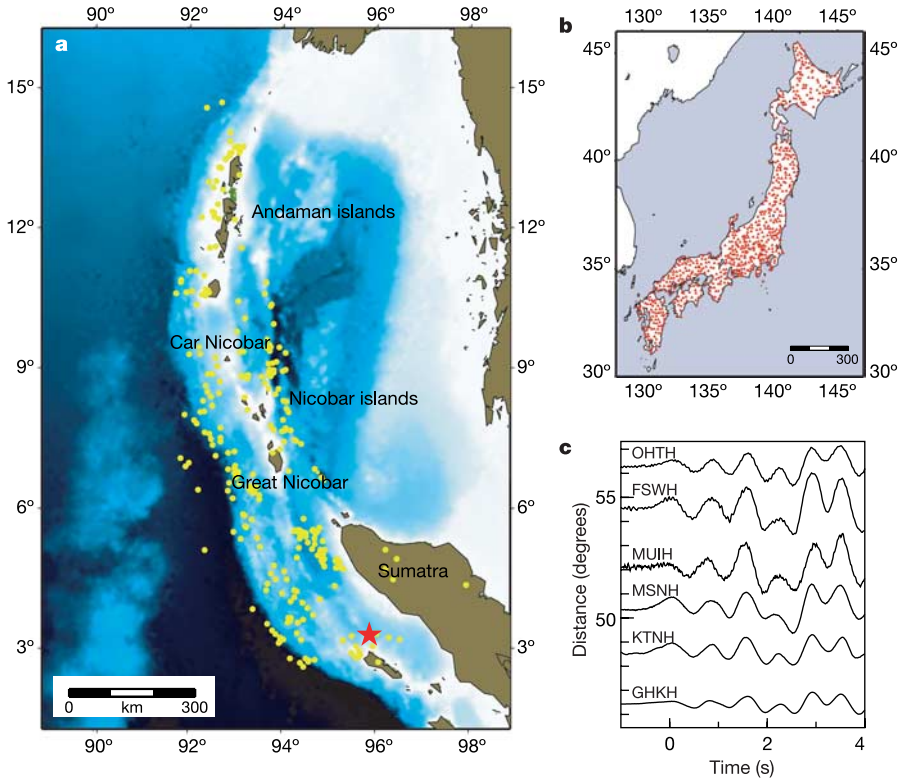

Figure 1 | Earthquake and station distribution. **a**, The region of the 26 December 2004 earthquake epicentre (red star) and aftershock locations (yellow dots). Seafloor bathymetry is shown as the background, with lighter colours for shallower regions. **b**, Distribution of ~700 stations (small red triangles) throughout Japan that comprise the Hi-Net seismic array. **c**, Examples of the initial (4 s) P-wave arrivals recorded on the vertical components at varying distances from the hypocentre. Station names are given with each trace.

[1]Institute of Geophysics and Planetary Physics, Scripps Institution of Oceanography, IGPP 0225, University of California San Diego, La Jolla, California 92093, USA. [2]Department of Earth and Space Sciences, IGPP, University of California Los Angeles, 595 Charles Young Drive East, Los Angeles, California 90095, USA.
*These authors contributed equally to this work.

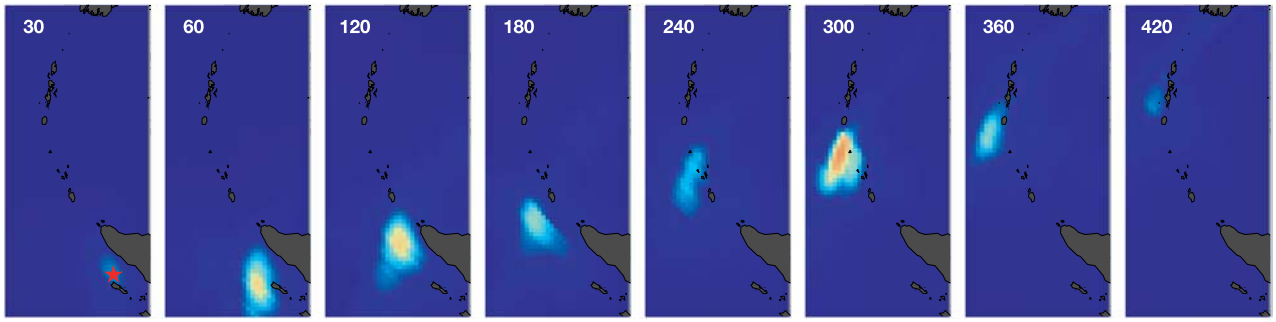

Figure 2 | Rupture progression. Maps showing the distribution of energy radiation at 30-s intervals for the first minute, and at 1-min intervals thereafter, following the earthquake initiation. Note the northward migration of the rupture during the ~8-min-long event. The epicentre is indicated by the red star in the first panel. The spacing for the source grid used to stack seismograms is 0.2° in both latitude and longitude.

times across the array, these complications can be unravelled to image the distribution of the high-frequency radiation during rupture.

Our analysis applies a back-projection method in which seismograms are stacked for each possible source location to obtain a direct image of the source[5,6] (see Methods). The stacking procedure sums the energy that is radiated from the given source point constructively, and cancels out other energy present in the seismograms. Resulting maps showing the squared amplitudes of the stacks, which are proportional to radiated seismic energy in the short-period band of the data (~1–5 s), are shown in Fig. 2 at progressive times, and the peak location and amplitude as a function of time are shown in Fig. 3. At time zero, the earthquake starts at the epicentre, just west of northern Sumatra. There is a major burst of radiated energy about 80 s later as the rupture progresses northwest (Fig. 3b). A second peak occurs at about 300 s, west of Car Nicobar where there was a tsunami-generating earthquake on 31 December 1881 with an estimated magnitude of 7.9 and a recurrence time of 114–200 yr (ref. 7). In the first 200 s, our analysis of high-frequency array data agrees with preliminary spatio-temporal slip-distribution models based on long-period global data. However, our rupture model lasts longer, for about 8 min (Fig. 3b), and extends farther to the north, into the Nicobar and Andaman islands region. The slip is unilateral with a sub-shear-wave speed of ~2.8 km s^{-1} (Fig. 3a).

To illustrate the total slip area, the distribution of cumulative

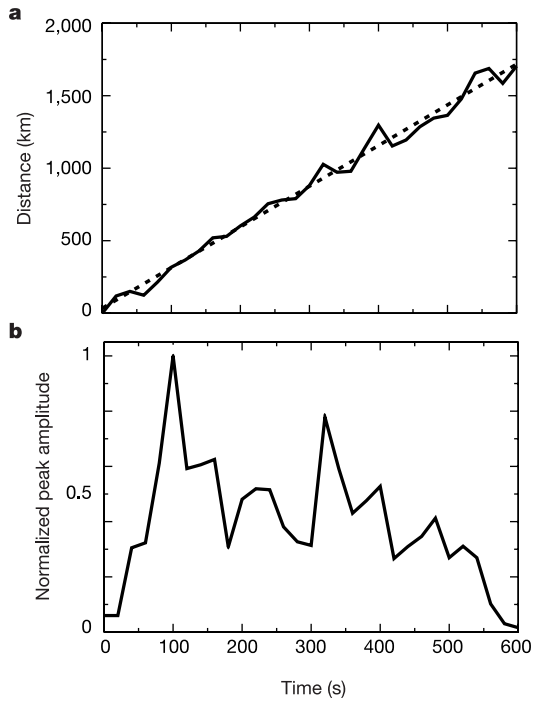

Figure 3 | Rupture speed and energy release. a, Rupture distance along the fault versus time. The dashed line is the straight-line fit to the peak locations, and gives an average rupture speed of 2.8 km s^{-1}. Distances beyond 1,300 km are not reliable because of the diminishing peak amplitudes beyond 500 s. **b**, Normalized peak amplitude as a function of time, showing two significant high-frequency energy events at ~80 s and 300 s.

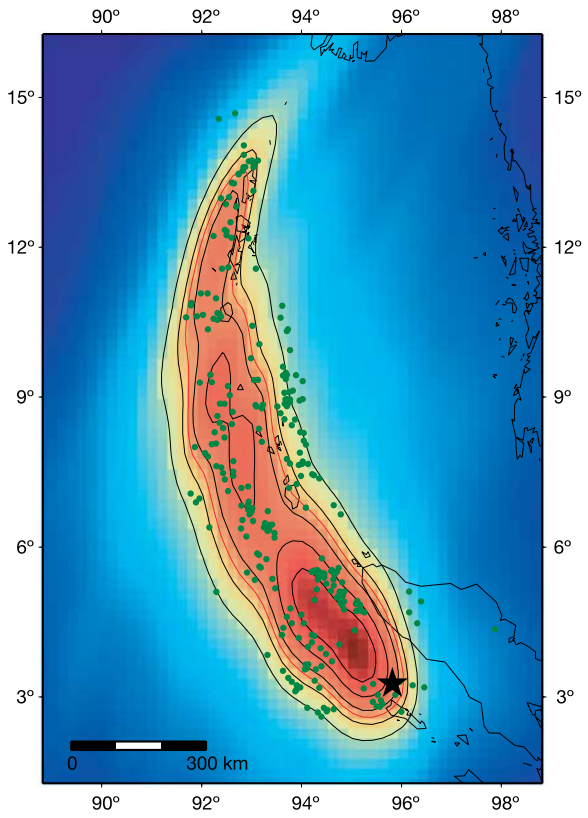

Figure 4 | Cumulative radiated energy. Integrated seismic energy over 600 s after initiation, normalized such that the maximum value is unity. The red contour, plotted at 65% of the maximum, encloses the slip area used to estimate the moment magnitude. The epicentre is shown as the black star. Note the good agreement between the 1,300-km-long rupture zone and the locations of the first month of aftershocks (dark green circles). The black contours are plotted at increments of 0.1 starting at 0.5. The image is computed and shown across the entire map, but amplitudes are very weak outside the contoured region.

radiated energy in the 600 s from the start of the earthquake is shown in Fig. 4. The slip is strongest in the southern portion west of northern Sumatra, but there is also significant radiation in the northern portion west of the Nicobar and Andaman islands. Because time shifts due to three-dimensional structure are derived from the initial waveforms associated with the hypocentre, the amplitudes towards the north end of the rupture are underestimated to some extent by incoherent stacking, and the northern peak may be as high as or higher than the southern peak. It is interesting to note that the largest aftershock (magnitude 7.1), 3.5 h after the mainshock, occurred west of Great Nicobar island where there is a local amplitude minimum in our model.

One test for the reliability of a rupture model is to compare its area to the aftershock distribution, because aftershocks generally occur near the mainshock slip surface. In Fig. 4, aftershock locations are shown by dark green circles, and their locations agree well with our image of the source of the high-frequency radiated energy. The 2004 Sumatra–Andaman earthquake has a comparable aftershock area to the three other largest earthquakes that have been adequately recorded; the 1957 Aleutian earthquake, the 1960 Chile earthquake, and the 1964 Alaskan earthquake (Fig. 5). The aftershock zones have markedly different aspect ratios owing to variations in rupture width and dip of the fault plane. Figure 5 demonstrates that the 2004 earthquake has the longest extent, about 1,300 km, consistent with our imaging. Similarly, the duration of rupture (about 500 s) is significantly longer than that of any known earthquake; average durations from short-period records for the Chile (13 stations) and Alaska (19 stations) events were ~345 s and ~340 s, respectively[8]. Estimates of rupture speed for the older earthquakes are somewhat uncertain but consistent; Chile broke dominantly unilaterally at ~3.5 km s^{-1} (ref. 9), Alaska broke unilaterally at ~3.0 km s^{-1} (ref. 10), and the Aleutian was largely unilateral with poorly constrained rupture speed[11]. Farther west along the Aleutian arc, the 1965 Rat islands earthquake with moment magnitude ~8.7 ruptured at 2.7–2.9 km s^{-1} (ref. 12). Unilateral rupture is a general tendency of large earthquakes[13], and the sub-shear-wave speeds of these earthquakes are roughly consistent with predictions for mode III crack propagation[14].

Slip area can provide a quick but crude estimate of seismic moment. We estimate from our imaging results that the slip area of the Sumatra–Andaman event was about 210,000 km^2 (area enclosed by the red contour on Fig. 4). The area defined by the first month of aftershocks is about 360,000 km^2. To correct for the expansion of the aftershock zone following a mainshock, this is reduced by a factor of 1.75 (ref. 15), resulting in a 1-day aftershock area of about 206,000 km^2, in agreement with our imaging result. Using an empirical relation[15], these areas yield a moment of ~1.3×10^{23} N m and moment magnitude ~9.3, in accord with recent normal-mode analysis[2]. Thus, in slip area, the Sumatra earthquake is second only to the 1960 Chile event among great earthquakes in the last 100 yr, whereas in length and duration, it exceeds all historical events. However, the value for the moment will ultimately require reconciliation of long-period seismic constraints on the fault slip with the high-frequency rupture surface, geodetic measurements and tsunami modelling.

Our model provides the most detailed view yet of rupture propagation in a great earthquake, aided by the long fault plane and the favourable location of the Hi-Net array. The large-scale features of the earthquake appear simple: a unilateral slip with an average speed of about 2.8 km s^{-1} and no secondary rupture. The long extent of the slip is also consistent with geodetic observations of island uplift and subsidence, which require substantial fault slip to the north (http://cires.colorado.edu/~bilham/IndonesiAndaman2004.htm). Because high-frequency radiation is likely to be accompanied by significant fault slip and moment release[8], we find no evidence to support the slow slip model hypothesized for the northern part of the rupture[2].

One of the advantages of this array approach is that it requires no prior knowledge of fault geometry, fault dimension, or rupture duration. In addition, this observation-driven method takes advantage of the entire P wavetrain, and calculation of synthetic seismograms is not needed. It is insensitive to interference from later seismic phases such as PP, because their angle of incidence across the array is different from that of direct P, and short-period PP amplitudes are also significantly less than direct P, owing to strong upper-mantle attenuation[3,16]. Finally, our approach provides more-detailed images of rupture timing and extent than are given by simple measures of short-period P-wave duration versus azimuth[3]. The success of our method for imaging the Sumatra–Andaman earthquake may, however, depend on the large dimensions of the earthquake and the large

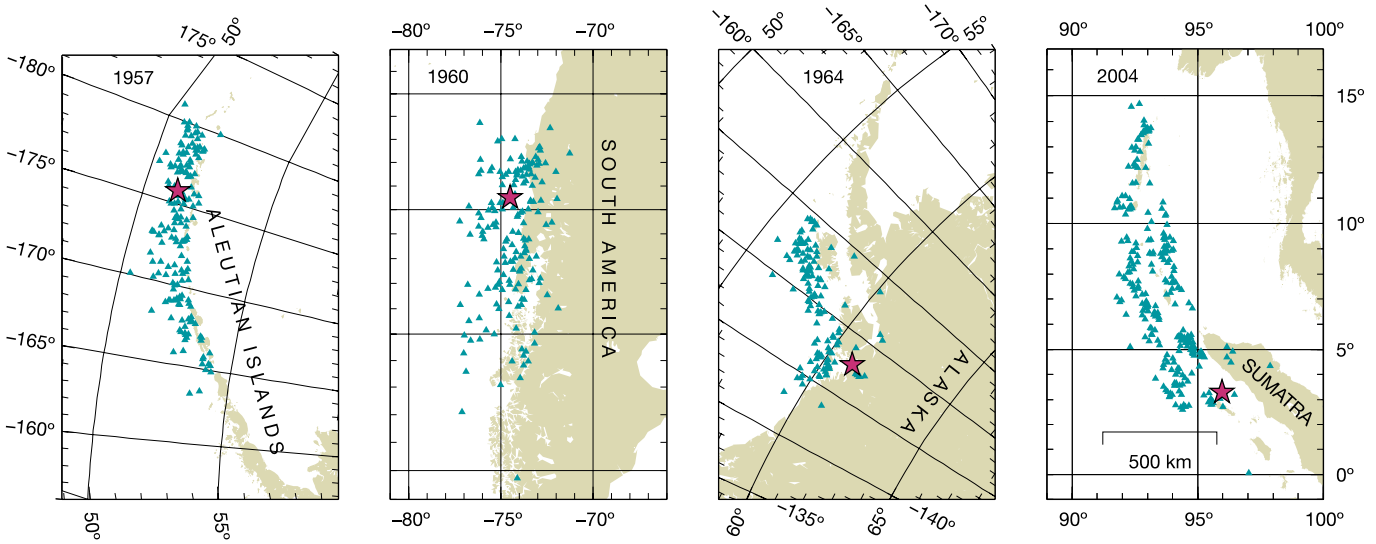

Figure 5 | Comparison of aftershock zones of great earthquakes. The epicentre of the mainshock is given by a red star, and aftershocks from the first month following the event are shown by blue-green triangles. All maps are at the same scale. The 2004 Sumatra–Andaman event has the longest aftershock zone, and an implied slip region that exceeds that of the 1957 $M_w \approx 9.0$ Aleutian[18] and 1964 $M_w \approx 9.2$ Alaska[19] events, and approaches that of the 1960 $M_w \approx 9.5$ Chile earthquake[20]. For 1964 and 2004, all aftershocks of $M_w \geq 5$ are included; all available aftershocks are included for 1957 and 1960 as most events have no magnitude estimates.

number of high-quality records that were available for our study; its usefulness for smaller earthquakes or sparser networks is not yet clear.

Our results demonstrate the value of dense, high-quality seismic arrays, such as the Japanese Hi-Net, for monitoring global as well as local seismicity. Because our method applies to the first arriving P waves, it could be implemented in a real-time system in which a good estimate of the length and duration of great earthquakes could be obtained within 20 to 30 minutes of the earthquake origin time, depending on the distance of the array from the event. Such a system could be achieved at relatively modest cost, and would be a valuable component of worldwide tsunami warning programmes.

METHODS

Our back-projection method is a simplification of wavefield reverse-time migration, a tool for imaging structure in reflection seismology. For the jth source location, the seismograms are summed to make the stack s_j as a function of time t:

$$s_j(t) = \sum\nolimits_k (p_k/A_k) u_k(t - t^p_{jk} + \Delta t_k)$$

where $u_k(t)$ is the vertical-component seismogram recorded at the kth station, and t^p_{jk} is the theoretical P-wave travel time from the jth source to the kth station[17]. Δt_k denotes timing corrections obtained from waveform cross-correlation of the initial 4 s of the P waves, which are used to enhance the coherence of the traces by accounting for effects due to three-dimensional structure. Finally, p_k and A_k are the polarity and amplitude of the seismograms obtained through cross-correlation analysis; the division by A_k ensures that the traces have approximately equal weight. The stacking procedure sums the energy that is radiated from the given source point constructively, and cancels out other energy present in the seismograms.

The records are de-meaned, but no other filter is applied. To ensure waveform similarity, only seismograms with a correlation coefficient for the first 4 s of the P wave of greater than 0.7 with respect to a simple waveform stack are included in the analysis. This cut-off gives 538 seismograms out of 686 available traces. The stacking is performed over an evenly spaced grid of source latitude and longitude at 0.2° intervals, assuming a constant depth of 30 km. Differences in expected amplitudes from geometrical spreading, source depth variations and directivity effects are ignored, but they should be relatively minor. Estimates of the width of the rupture and the slip duration at fixed points are limited by the array geometry and the frequency content of the data (see Supplementary Information). The spatial resolution depends on the location, but the uncertainty in the rupture area generally takes the form of a 60 km by 170 km ellipse. The uncertainty in the rupture duration at fixed points along the fault is about 20 s.

Received 13 February; accepted 18 April 2005.
Published online 22 May 2005.

1. Dziewonski, A. M. & Woodhouse, J. H. An experiment in systematic study of global seismicity: Centroid-moment tensor solutions for 201 moderate and large earthquakes of 1981. *J. Geophys. Res.* **88,** 3247–3271 (1983).
2. Stein, S. & Okal, E. A. Speed and size of the Sumatra earthquake. *Nature* **434,** 581–582 (2005).
3. Ni, S., Kanamori, H. & Helmberger, D. Energy radiation from the Sumatra earthquake. *Nature* **434,** 582 (2005).
4. National Research Institute for Earth Science and Disaster Prevention. ⟨http://www.hinet.bosai.go.jp⟩ (2005).
5. Ellsworth, W. L. Imaging fault rupture without inversion. *Seismol. Res. Lett.* **63,** 73 (1992).
6. Spudich, P. & Cranswick, E. Direct observation of rupture propagation during the Imperial Valley earthquake using a short baseline accelerometer array. *Bull. Seismol. Soc. Am.* **74,** 2083–2114 (1984).
7. Ortiz, M. & Bilham, R. Source area and rupture parameters of the 31 December 1881 Mw = 7.9 Car Nicobar earthquake estimated from tsunamis recorded in the Bay of Bengal. *J. Geophys. Res.* **108** (2003) doi:10.1029/2002JB001941.
8. Houston, H. & Kanamori, H. Source spectra of great earthquakes: Teleseismic constraints on rupture process and strong ground motion. *Bull. Seismol. Soc. Am.* **76,** 19–42 (1986).
9. Kanamori, H. & Cipar, J. J. Focal process of the great Chilean earthquake May 22, 1960. *Phys. Earth Planet. Inter.* **9,** 128–136 (1974).
10. Christensen, D. H. & Beck, S. L. The rupture process and tectonic implications of the great 1964 Prince-William-Sound earthquake. *Pure Appl. Geophys.* **142,** 29–53 (1994).
11. Johnson, J. M. *et al.* The 1957 great Aleutian earthquake. *Pure Appl. Geophys.* **142,** 3–28 (1994).
12. Beck, S. L. & Christensen, D. H. Rupture process of the February 4, 1965, Rat Islands earthquake. *J. Geophys. Res.* **96,** 2205–2221 (1991).
13. McGuire, J. J., Zhao, L. & Jordan, T. H. Predominance of unilateral rupture for a global catalog of large earthquakes. *Bull. Seismol. Soc. Am.* **92,** 3309–3317 (2002).
14. Kanamori, H. & Brodsky, E. E. The physics of earthquakes. *Rep. Prog. Phys.* **67,** 1429–1496 (2004).
15. Kanamori, H. The energy release in great earthquakes. *J. Geophys. Res.* **82,** 2981–2987 (1977).
16. Shearer, P. M. & Earle, P. S. The global short-period wavefield modelled with a Monte Carlo seismic phonon method. *Geophys. J. Int.* **158,** 1103–1117 (2004).
17. Kennett, B. L. N. *IASPEI 1991 Seismological Tables* (Research School of Earth Sciences, Australia National University, Canberra, Australia, 1991).
18. Brazee, R. J. & Cloud, W. K. *United States Earthquakes 1957* (US Coast and Geodetic Survey, Washington DC, 1959).
19. Algermissen, S. T., Rinehart, W. A., Sherburne, R. W. & Dillinger, W. H. *The Great Alaska Earthquake of 1964* 313–364 (National Academy of Sciences, Washington DC, 1972).
20. Talley, J. H. C. & Cloud, W. K. *United States Earthquakes 1960* (US Coast and Geodetic Survey, Washington DC, 1962).

Supplementary Information is linked to the online version of the paper at www.nature.com/nature.

Acknowledgements We thank the National Research Institute for Earth Science and Disaster Prevention in Japan for making the Hi-Net data available on the Internet.

Author Information Reprints and permissions information is available at npg.nature.com/reprintsandpermissions. The authors declare no competing financial interests. Correspondence and requests for materials should be addressed to M.I. (mishii@ucsd.edu).